Sensors & Actuators: B. Chemical 443 (2025) 138179

Contents lists available at ScienceDirect

Sensors and Actuators: B. Chemical

journal homepage: www.elsevier.com/locate/snb

Electrochemiluminescence sensor based on the quenching effect of MOF-199 nanomaterials towards ternary semiconductor $CdIn_2S_4$ for sensitive analysis of D-dimers

Fengdi Li [a], Yun Wang [a], Hao Yu [a], Xianpeng Liao [a], Kailong Liu [a], Lihua Hu [a,*], Hongmin Ma [a], Dan Wu [a], Qin Wei [a,b,**], Huangxian Ju [a,c]

[a] Collaborative Innovation Center for Green Chemical Manufacturing and Accurate Detection, Key Laboratory of Interfacial Reaction & Sensing Analysis in Universities of Shandong, School of Chemistry and Chemical Engineering, University of Jinan, Jinan 250022, PR China
[b] Department of Chemistry, Sungkyunkwan University, Suwon 16419, Republic of Korea
[c] State Key Laboratory of Analytical Chemistry for Life Science, School of Chemistry and Chemical Engineering, Nanjing University, Nanjing 210023, PR China

ARTICLE INFO

Keywords:
Electrochemiluminescence
$CdIn_2S_4$
Dual quenching
D-dimer

ABSTRACT

Ternary metal sulfide semiconductors demonstrate considerable potential for electrochemiluminescence (ECL) applications, because of their high charge carrier mobility and good stability. Herein, $CdIn_2S_4$ was innovatively employed as a luminescent material owing to its excellent near-infrared (NIR) ECL emission. Its narrow bandgap, excellent solubility, and stability in aqueous solutions prevented electrode passivation and enhanced the ECL intensity, efficiency, and stability. The MOF-199 nanomaterial featuring a pyramid structure was employed as a quenching probe, exhibiting a dual-quenching effect based on electron and ECL energy transfers, facilitated by energy-level matching and spectral overlapping with luminescent $CdIn_2S_4$. The dual-quenching strategy considerably enhanced the quenching efficiency of the probe. Therefore, based on $CdIn_2S_4$ exhibiting an excellent luminescence performance and MOF-199 demonstrating an exceptional quenching effect, a novel quenching-type sandwich immunosensor was developed for the sensitive detection of D-dimers. The detection limit of the sensor was 8.51 fg/mL. Furthermore, the sensor exhibited excellent specificity, reproducibility, and stability. The proposed approach offers a novel theoretical framework and methodological guidance for the detection of biomarkers and, provides valuable insights for the development of new luminescent materials.

1. Introduction

D-dimers, the byproducts of fibrin degradation, function as signaling molecules in plasma to activate the coagulation system. In fibrinolysis, plasma D-dimers are widely recognized as the definitive markers of secondary fibrinolysis, particularly for ruling out venous thrombosis, pulmonary embolism, diffuse intravascular coagulation, and related diseases. The clinical stage of cancer is associated with increased serum D-dimer levels, which are recognized as diagnostic and prognostic indicators for various cancers[1,2]. Several methodologies have been developed for identifying D-dimers, including whole blood agglutination, enzyme-linked immunosorbent assay, immunoturbidimetric assay, and chemiluminescent assay[3]. Despite the advantages the application of these methods is limited owing to various challenges. At present, electrochemiluminescence (ECL) immunoassay based on the antibody-specific recognition of the target is among the most reliable assays under study. During ECL, a substance undergoes electron transfer on an electrode surface to create an excited state, leading to luminescence[4–6]. ECL immunosensors are used in biosensing analysis because of their high sensitivity, wide dynamic response range, low signal-to-noise ratio, and easy control. Therefore, they are ideal for detecting D-dimers.

Diverse binary semiconductor materials, including CdS, CdSe, CdTe and ZnSe, have been identified as potential ECL emitters, and are currently under active investigation for their potential bioanalytical applications in various fields[7–9]. The ternary semiconductor

* Corresponding author.
** Corresponding author at: Collaborative Innovation Center for Green Chemical Manufacturing and Accurate Detection, Key Laboratory of Interfacial Reaction & Sensing Analysis in Universities of Shandong, School of Chemistry and Chemical Engineering, University of Jinan, Jinan 250022, PR China.
E-mail addresses: hulihua1206@163.com (L. Hu), sdjndxwq@163.com (Q. Wei).

https://doi.org/10.1016/j.snb.2025.138179
Received 27 February 2025; Received in revised form 21 June 2025; Accepted 23 June 2025
Available online 28 June 2025

compound AB_mC_n possesses a chalcopyrite structure. Sulfides, selenides, and stable metals containing elements featuring the d10 electronic configuration (e.g., Cd, Zn, and In) exhibit favorable photoexcited carrier mobility, as their conduction bands comprise hybridized and widely dispersed sp orbitals[10]. $CdIn_2S_4$ is a ternary semiconductor material possessing an AB_2X_4-type cubic spinel structure, in which indium ions are chemically stable, featuring tetrahedral and octahedral coordination. Compared with conventional binary metal sulfides, $CdIn_2S_4$ possesses superior light-absorption performance and stability and, is widely used in optoelectronics, sensing, and photocatalysis. $CdIn_2S_4$ has a narrow bandgap and adaptable optical characteristics, providing new opportunities for innovative ECL emitters. $CdIn_2S_4$ demonstrates excellent multichannel ECL behavior in aqueous solutions exhibiting high emission intensity, which is attributed to the point defects in the material promoting efficient electron-hole complexation[11]. When $K_2S_2O_8$ is used as a co-reactant, $CdIn_2S_4$ demonstrates intense near-infrared (NIR) ECL emission and high luminescent stability. Experimentally, the ECL emission mechanism in $CdIn_2S_4$ is based on surface-state transitions. $CdIn_2S_4$ exhibits excellent NIR characteristics, and the NIR ECL features enable the advantageous properties of low photochemical damage, high tissue permeability, and minimal background interference. NIR ECL luminophores have attracted considerable attention in bioimaging and diagnostics. $CdIn_2S_4$ exhibits has good application prospects in ECL sensing and bioimaging.

In addition to the design of efficient luminescent materials, a key requirement for the fabrication of quenching-type ECL sensors is the development of high-performance quenching probes. Furthermore, an efficient quenching mechanism is particularly important. Typically, resonance energy transfer is the common mode of quenching, and effective quenching can be achieved when the distance is sufficiently small and an effective spectral overlap exists between the donor and acceptor[12–14]. The dual-quenching effect can notably improve the quenching efficiency under the synergistic action of electron and energy transfers[15–17]. Polyoxomolybdate–zirconia (POM-ZrO_2) is a novel ECL luminescent material featuring strong and stable ECL signals[18]. Furthermore, using polyaniline@Au nanocrystals (PANI@AuNPs) as a quencher, the quenching efficiency considerably enhances through a dual mechanism involving energy and electron transfers.

Metal-organic frameworks (MOFs) represent a crucial class of porous materials, and their pore dimensions and compositions are highly controllable. Their high porosity is pivotal for applications such as separation, catalysis, and sensing. MOFs are characterized by high selectivity, stability at low medium temperatures, moderate adsorption heat, and improved mass uptake, rendering them advantageous compared with other porous materials. MOF-199 is a typical nanoporous material possessing a double-pyramid structure, which is formed by the coordination of 1,3,5-benzene tricarboxylic acid with Cu^{2+} [19,20]. MOF-199 has high stability, high porosity, large specific surface area, and abundant surface carboxyl groups, thereby imparting good biocompatibility and facilitating its conjugation with biological molecules, such as antibodies. Furthermore, MOF-199 exhibits strong ability for energy-level alignment with $CdIn_2S_4$, concerning electron transfer. Additionally, its ultraviolet (UV) absorption spectrum exhibits a certain degree of overlap with the ECL emission spectrum of $CdIn_2S_4$ therefore, MOF-199 can be utilized as an energy acceptor to effectively quench the ECL of $CdIn_2S_4$. This material can be applied as a high-efficiency quenching probe, operating based on the double-quenching effect.

This study developed a sandwich-type ECL biosensor employing a novel $CdIn_2S_4$ emitter and MOF-199 nanoparticles as signal quenching probes for, the ultrasensitive detection of D-dimers. The $CdIn_2S_4$ emitter demonstrates robust and stable ECL emission, exhibiting enhanced biocompatibility through amination modification. The MOF-199 nanomaterial effectively binds with antibodies and efficiently quenches the ECL signal of the luminescent emitter through a dual mechanism involving electron transfer and energy transfer, enhancing the stability of the system. The developed biosensor demonstrates an excellent linear detection range of 0.00005–100 ng/mL, exhibiting a substantially low detection limit of 8.51 fg/mL (S/N = 3). This study presents a novel theoretical framework and methodological approach for the clinical analysis of various biomolecules and, valuable insights into the design of new-generation luminescent materials.

2. Experimental section

2.1. Materials and apparatus

The details of the materials and apparatus used are provided in the Supplementary Material.

2.2. Preparation of $CdIn_2S_4$-NH_2

First, $CdIn_2S_4$ was synthesized following a previously reported method[21]. At room temperature, $CdCl_2{\cdot}2.5\ H_2O$ (228.36 mg) and $InCl_3$ (442.34 mg) were dispersed in water (60 mL) and continuously stirred for 30 min. Subsequently, thioacetamide (TAA, 601.06 mg) was added to the as-prepared mixture and stirred for an additional 30 min at room temperature. The homogeneous solution was transferred to a 100 mL Teflon-lined stainless-steel autoclave, sealed, and subjected to hydrothermal treatment at 180 ℃ for 24 h. The resulting suspension was centrifuged at 8000 rpm for 5 min, separately washed with deionized water and anhydrous ethanol three times, and finally dried in a vacuum oven at 60 ℃ for 12 h to successfully obtain $CdIn_2S_4$ microspheres.

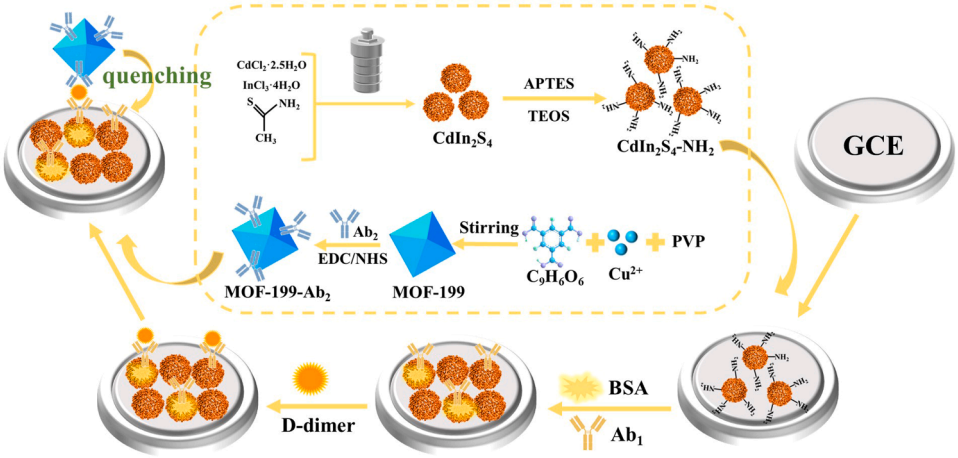

Scheme 1. Fabrication of the immunosensor for D-dimer detection.

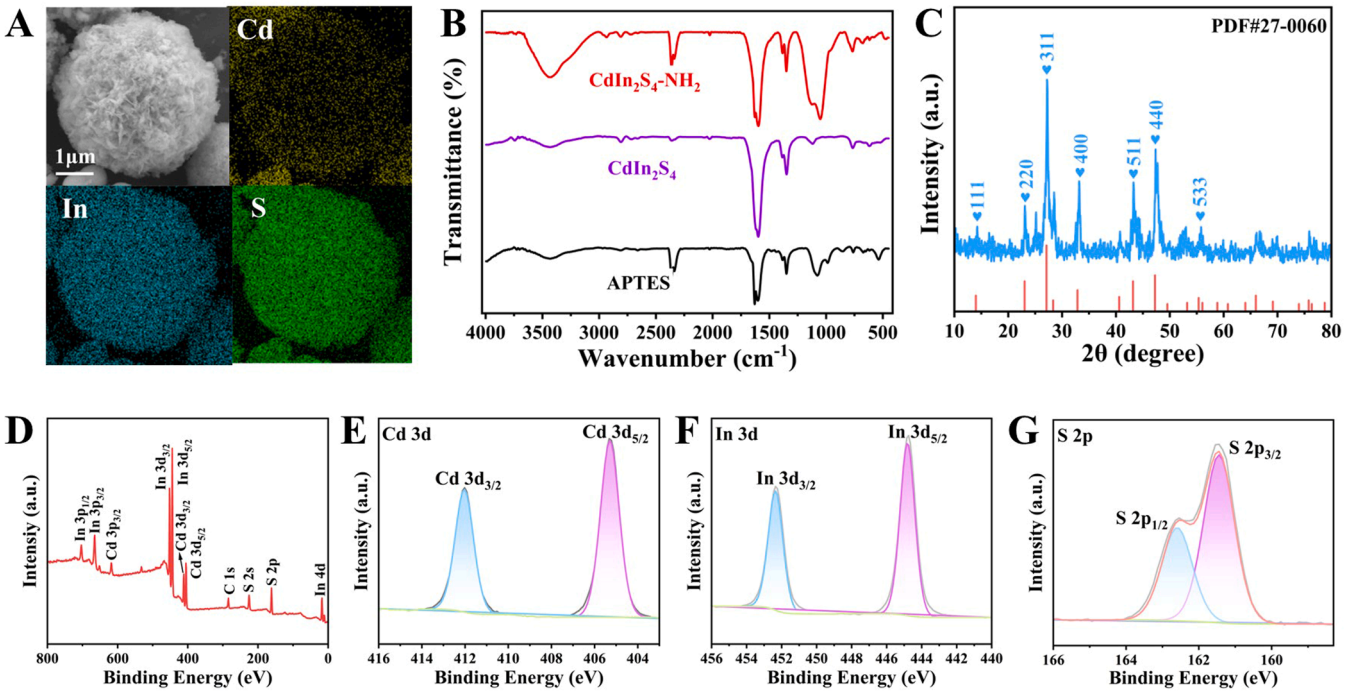

Fig. 1. SEM images of (A) $CdIn_2S_4$. (B) FT-IR spectra of APTES, $CdIn_2S_4$ and $CdIn_2S_4$-NH_2. (C) XRD pattern of $CdIn_2S_4$. (D) XPS spectrum of $CdIn_2S_4$, (E) Cd 3d, (F) In 3d spectrum and (G) S 2p spectra.

Next, $CdIn_2S_4$ was aminated with (3-aminopropyl) triethoxysilane (APTES)[22], and 100 mg of $CdIn_2S_4$ was dissolved in 80 % ethanol solution and sonicated to form a homogeneous $CdIn_2S_4$ suspension (1 mg/mL). Thereafter, 1 mL of concentrated ammonia was added to the suspension. Subsequently, 67 μL of tetraethyl orthosilicate (TEOS) and 67 μL of APTES were added dropwise to the $CdIn_2S_4$ suspension, and the mixture was magnetically stirred at 35 ℃ for 3 h. The resulting suspension was centrifuged at 8000 rpm for 5 min, separately washed with deionized water and anhydrous ethanol three times, and finally dried in a vacuum oven at 60 ℃ for 12 h. Accordingly, $CdIn_2S_4$-NH_2 was synthesized, exhibiting higher biocompatibility than $CdIn_2S_4$.

2.3. Preparation of MOF-199-Ab_2

MOF-199 was synthesized based on previously reported methods with certain modifications[23]. At room temperature, $Cu(NO_3)_2{\cdot}3\ H_2O$ (0.9 g) and polyvinylpyrrolidone (PVP, 0.4 g) were dissolved in methanol (50 mL) via stirring. Next, 50 mL of a methanol solution containing 1,3,5-benzenetricarboxylic acid (0.43 g) was added to the as-prepared solution in incremental amounts, obtaining a blue colloidal suspension. After stirring for 10 min, the colloidal mixture was left to stand at room temperature for 24 h. The resulting crystals were centrifuged at 8000 rpm for 5 min and washed with methanol three times. Subsequently, the as-formed blue crystalline precipitate was dried in vacuum at 60 ℃ for 12 h to obtain MOF-199 octahedra.

Next, 50 μL of the D-dimer of Ab_2 (10 μg/mL) was dispersed in 1 mL of phosphate-buffered saline (PBS) solution, and 1-(3-dimethylaminopropyl)-3-ethylcarbodiimide (EDC, 76 mg), N-hydroxy succinimide (NHS, 11.5 mg) were added, followed by shaking at 4 ℃ for 4 h. Thereafter, 2 mg of the MOF-199 solid powder was added to the aforementioned solution and subsequently incubated for 12 h at 4 ℃ under shaking. After centrifugation, the resulting material was dispersed in 1 mL of PBS (pH = 7.4) and stored at 4 ℃.

2.4. Fabrication of the ECL immunosensor

A schematic of immunosensor fabrication on a 4 mm diameter glassy carbon electrode (GCE) is illustrated in Scheme 1. Initially, the GCE was meticulously polished using 0.05 μm alumina paste, followed by thorough cleansing with ultrapure water to ensure optimal surface smoothness. Next, 6 μL of the 2 mg/mL $CdIn_2S_4$-NH_2 solution was deposited onto the polished GCE and air-dried at room temperature. Thereafter, 6 μL of Ab_1 (10 μg/mL) was complexed onto the electrode and with PBS (pH 7.4). Afterward, 3 μL of bovine serum albumin (BSA, 0.1 wt%) was utilized to block the nonspecific binding sites, and the electrode was subsequently rinsed with PBS. Thereafter, different concentrations of D-dimers were applied to the electrode surface, followed by incubation at 4 ℃ for 4 h. Subsequently, the electrodes were rinsed with PBS. Finally, 6 μL of MOF-199-Ab_2 was incubated on the electrode, and the biosensor was stored at 4 ℃ for subsequent use.

3. Results and discussion

3.1. Characterization of materials

The morphology of the materials was characterized by scanning electron microscopy (SEM). As shown in Fig. S1A and S1B, $CdIn_2S_4$ presents a uniform spherical morphology and an irregular surface texture. Its size is almost uniformly distributed in the range of 4 −7 μm. Fig. 1A illustrates the energy-dispersive X-ray spectroscopy (EDS) elemental mapping representative image of $CdIn_2S_4$, in which Cd, In, and S elements are distinctly observed. Furthermore, the elemental mapping distribution profile of $CdIn_2S_4$ indicates the successful synthesis of $CdIn_2S_4$ (Fig. S1C).

The Fourier transform infrared (FT-IR) spectroscopy analysis was conducted to determine the functional groups of APTES, $CdIn_2S_4$, and $CdIn_2S_4$-NH_2 (Fig. 1B). For pure $CdIn_2S_4$, the peak at 3427 cm^{-1} is related to the –OH group on the $CdIn_2S_4$ surface. The FT-IR spectrum of APTES-functionalized $CdIn_2S_4$ demonstrates several new characteristic peaks in addition to the typical peaks of $CdIn_2S_4$. The large characteristic

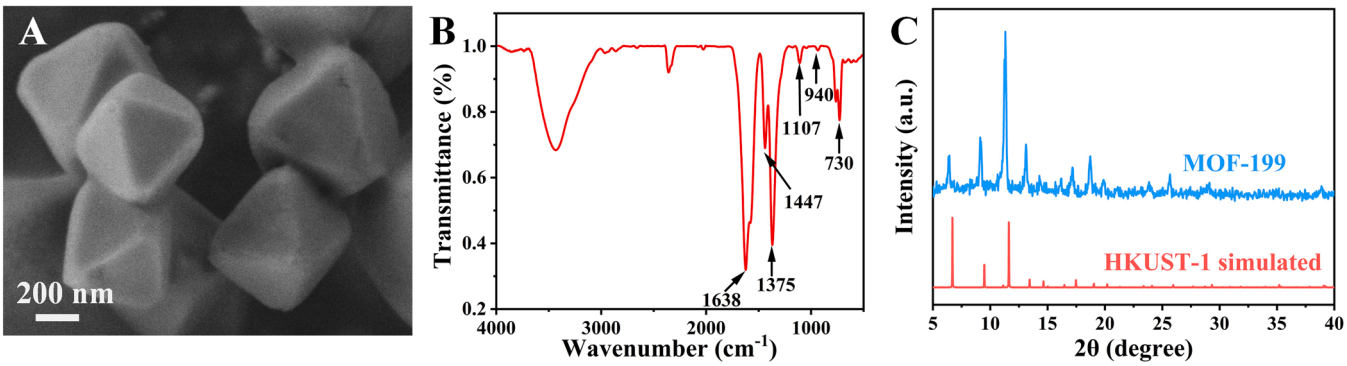

Fig. 2. (A) SEM image, (B) FT-IR spectrum, and (C) XRD pattern of MOF-199.

peaks within 3000 −3700 cm^{-1} correspond to the stretching vibration of the amino group. The peak at 2922 cm^{-1} is attributed to the C−H group of APTES, and those at 1114.5 and 500 cm^{-1} correspond to the Si−O−Si and Si−O−C stretching vibrations[24]. These finding confirm the successful coating of $CdIn_2S_4$ microspheres with APTES.

The crystal phase structure of $CdIn_2S_4$ was analyzed using the X-ray diffraction (XRD) pattern (Fig. 1C). The diffraction peaks and crystal faces of $CdIn_2S_4$ are highly consistent with those of a cubic spinel structure and the standard card PDF#27–0060. In the pure $CdIn_2S_4$ pattern, the main characteristic peaks are located at 14.2°, 23.2°, 27.3°, 33.1°, 43.3°, 47.5°, and 55.7°, corresponding to the (110), (220), (311), (400), (511), (440), and (533) planes[25].

A detailed X-ray photoelectron spectroscopy (XPS) analysis was conducted to determine the elemental composition of $CdIn_2S_4$. The $CdIn_2S_4$ full spectrum (Fig. 1D) reveals that $CdIn_2S_4$ comprises Cd, In, and S elements, which is consistent with the EDS results[26]. Moreover, the C peak in the full spectrum is attributed to the calibration standard carbon, whereas the O 1 s signal originates from the O_2 or H_2O molecules adsorbed on the sample[27]. The high-resolution Cd 3d XPS spectrum in Fig. 1E exhibits two distinct peaks at 411.9 eV and 406.03 eV, corresponding to Cd $3d_{3/2}$ and Cd $3d_{5/2}$ spin-orbit states. The difference in the binding energy between these two peaks is 5.87 eV, which is attributed to the energy level corresponding to Cd^{2+}, confirming that Cd exists as Cd^{2+} in the crystal[28]. In the high-resolution In 3d spectrum (Fig. 1F), the peaks at 453.02 eV and 446.01 eV correspond to In $3d_{3/2}$ and In $3d_{5/2}$ spin-orbit states, indicating that the oxidation state of In is + 3[29]. In the S 2p spectrum (Fig. 1G), the peaks at 162.2 eV and 161.9 eV are attributed to the S $2p_{1/2}$ and $2p_{3/2}$ spin-orbit states, respectively, indicating that sulfur exists as S^{2-} in $CdIn_2S_4$[30]. These results confirm the successful synthesis of $CdIn_2S_4$.

The morphology of MOF-199 was characterized by SEM. MOF-199, which is a blue powder, that utilizes PVP as a capping agent for maintaining coordination equilibrium on its crystal surface during synthesis. Fig. 2A displays the standard bipyramidal morphology of MOF-199, featuring a size of approximately 300 −500 nm, synthesized through the incremental addition of 1,3,5-benzenetricarboxylic acid to a copper nitrate solution. The bipyramidal units of MOF-199 are stacked to form an irregular structure. The morphological inhomogeneity of MOF-199 has been previously reported[31].

The surface groups of MOF-199 were examined by FT-IR spectroscopy. The FT-IR spectrum in Fig. 2B features distinct absorption bands corresponding to the predicted functional groups, confirming the presence of these groups within the MOF-199 structure. A broad peak is observed at 3100 −3600 cm^{-1}, which is attributed to the −OH groups of 1,3,5-benzenetricarboxylic acid, and weakly bound water molecules. The peak at 1638 cm^{-1} is attributed to asymmetric carboxylic acid, whereas the bands at 1447 and 1375 cm^{-1} correspond to the symmetric stretching vibrations of carboxylic acid. The absorption bands at 1107 and 940 cm^{-1} correspond to the in-plane and out-of-plane bending vibrations of the C−H bond. In addition, the peak at 730 cm^{-1} is attributed to the stretching vibrations of Cu−O, in which the oxygen atom is coordinated to Cu[32]. The aforementioned results further confirm the successful preparation of MOF-199.

As a structure-directing agent, PVP facilitates the crystallization of MOF structural domains by promoting the interactions between its pyrrolidone ring (C═O) and metal ions. The crystal structure of the synthesized MOF-199 was characterized using XRD. Fig. 2C presents the XRD pattern of MOF-199 and the simulated pattern of a previously reported material HKUST-1, demonstrating the similar crystallinity of MOF-199 and HKUST-1. The XRD data of MOF-199 closely matches the simulation results of HKUST-1, indicating good crystalline quality.

3.2. ECL emission behavior and MOF-199 quenching mechanism of the $CdIn_2S_4/K_2S_2O_8$ system

We explored the ECL emission mechanism of the $CdIn_2S_4/K_2S_2O_8$ system (Fig. S2A). Comparing the ECL and photoluminescence (PL) spectra of $CdIn_2S_4$ provided insights into its surface-state properties. Fig. S2B depicts the PL spectrum, peaking at 500 nm, and the ECL spectrum, exhibiting intense emission in a broad spectral range of 550 −750 nm, of $CdIn_2S_4$. Therefore, $CdIn_2S_4$ exhibits excellent NIR emission properties. The ECL spectrum is redshifted compared with the PL spectrum, therefore the generation of $CdIn_2S_4$* is inferred to be caused by the surface-state jump[33]. Considerably, the ECL emission mechanism of $CdIn_2S_4$ is elucidated as follows:

$$CdIn_2S_4 + e^- \rightarrow CdIn_2S_4^{\bullet -} \quad (1)$$

$$S_2O_8^{2-} + e^- \rightarrow SO_4^{2-} + SO_4^{\bullet -} \quad (2)$$

$$SO_4^{\bullet -} \rightarrow SO_4^{2-} + h^+ \quad (3)$$

$$CdIn_2S_4^{\bullet -} + SO_4^{\bullet -} \rightarrow SO_4^{2-} + CdIn_2S_4^* \quad (4)$$

$$CdIn_2S_4^* \rightarrow CdIn_2S_4 + h\nu \quad (5)$$

When the scanning potential is sufficiently negative, $CdIn_2S_4$ reduces to $CdIn_2S_4^{\bullet -}$ (Eq. 1). Meanwhile, $S_2O_8^{2-}$ reduces to $SO_4^{\bullet -}$ (Eq. 2). The as-formed $SO_4^{\bullet -}$ injects holes into the valence band of $CdIn_2S_4$ (Eq. 3). $CdIn_2S_4^{\bullet -}$ readily reacts with the strong oxidant $SO_4^{\bullet -}$ to form $CdIn_2S_4$* (Eq. 4). Finally, when $CdIn_2S_4$* returns from the excited to the ground state as a photon, strong light emission occurs, resulting in ECL emission (Eq. 5).

To demonstrate $CdIn_2S_4$ as a co-reactive ECL luminophore, the function of $K_2S_2O_8$ in this system was investigated using cyclic voltammogram. In Fig. S2C, no clear reduction peak of $CdIn_2S_4$ is obtained in the PBS solution in the scanning potential of −1.5 −0 V (curve a), whereas in the PBS solution containing $K_2S_2O_8$, a reduction peak of GCE is obtained at −0.62 V (curve b), which is attributed to the electrochemical reduction of the $K_2S_2O_8$ co-reactant. Furthermore, the reduction peak of $CdIn_2S_4$/GCE is obtained in the PBS solution containing $K_2S_2O_8$ at −1.37 V, and the current increases (curve c), which is

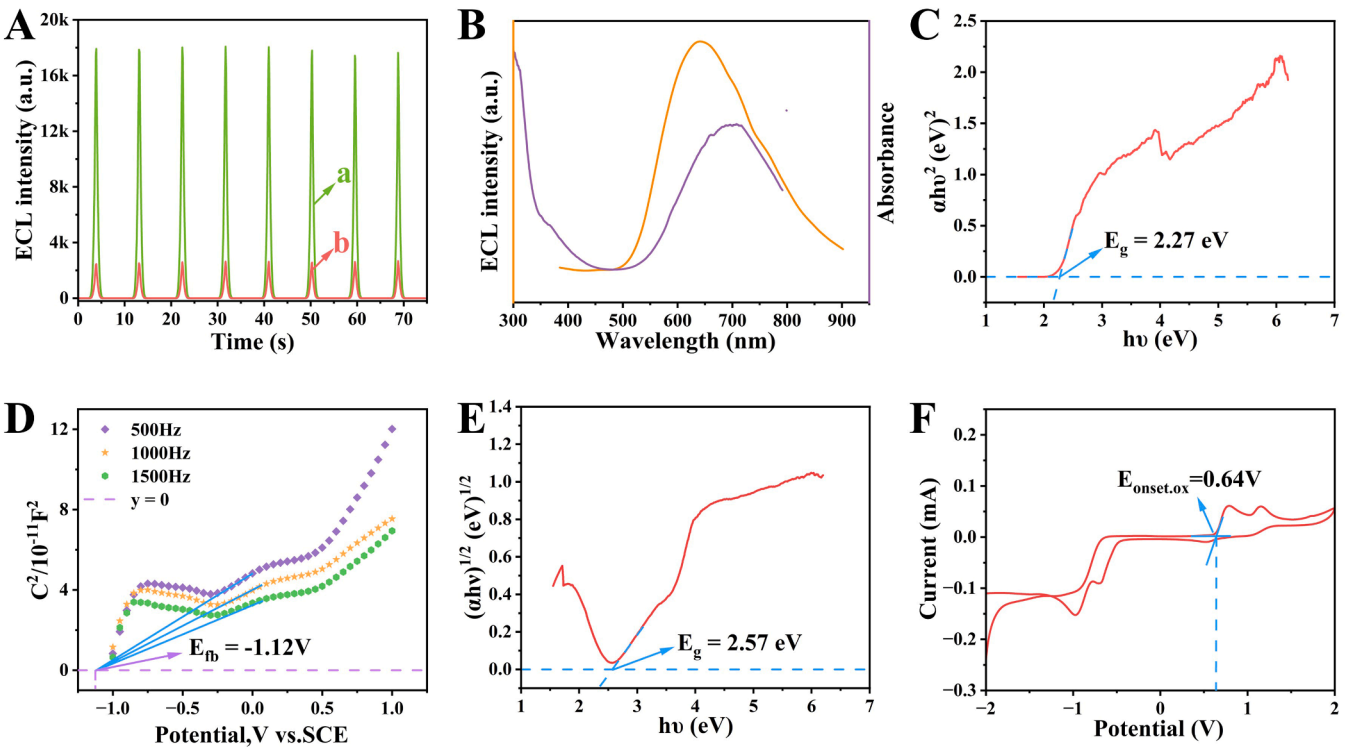

Fig. 3. (A) ECL intensity of GCE/$CdIn_2S_4$-NH_2 (curve a) and GCE/ $CdIn_2S_4$-NH_2/MOF-199 (curve b). (B) ECL emission spectrum of $CdIn_2S_4$ and UV–vis absorption spectrum of MOF-199. (C) UV–vis DRS spectrum of $CdIn_2S_4$. (D) M-S curves of the $CdIn_2S_4$ samples, (E) UV–vis DRS spectrum, and (F) cyclic voltammogram of MOF-199.

attributed to the semiconductor characteristics of $CdIn_2S_4$.

Additionally, we explored the quenching mechanism of the immunosensor. ECL measurements were conducted using the GCE/$CdIn_2S_4$-NH_2 (curve a) and GCE/$CdIn_2S_4$-NH_2/MOF-199 (curve b) electrodes. Fig. 3A demonstrates that the ECL signal of the novel luminescent $CdIn_2S_4$-NH_2 considerably decreases when the GCE is modified with MOF-199.

The present study proposes a dual-quenching mechanism involving the transfer of energy and electrons. The ECL emission spectrum of $CdIn_2S_4$-NH_2 exhibits broad, bright ECL emission at wavelength 550 −750 nm, and MOF-199 exhibits UV absorption within 600 −750 nm (Fig. 3B). Therefore, the ECL spectrum of $CdIn_2S_4$-NH_2 partially overlaps with the UV–vis absorbance spectrum of MOF-199, facilitating ECL energy transfer[34,35]. Furthermore, the energy levels of the $CdIn_2S_4$-NH_2 luminophores were investigated by UV−vis diffuse reflectance spectroscopy (DRS) and Mott–Schottky (M–S) analyses. The results obtained by the UV−vis DRS spectrum of $CdIn_2S_4$-NH_2 presented in Fig. 3C, revealing that the bandgap energy of $CdIn_2S_4$-NH_2 is estimated to be E_g = 2.27 eV. The flat-band potential of $CdIn_2S_4$-NH_2 can be derived from the intercept of the tangent line in the M–S plot (Fig. 3D). Because $CdIn_2S_4$-NH_2 is an n-type semiconductor, its flat-band potential can be directly considered as the conduction-band position[36–38], leading to E_{CB} = -1.12 V and E_{VB} = -3.39 V. The UV–vis DRS spectrum of MOF-199 is depicted in Fig. 3E, from which the bandgap energy is calculated to be Eg = 2.57 eV. The highest occupied molecular orbital and lowest unoccupied molecular orbital energy levels of MOF-199 were determined by cyclic voltammetry. Based on the cyclic voltammogram (Fig. 3F), we obtained φ_{ox} = 0.64 eV, and further obtained therefore E_{HOMO} = -5 eV. The aforementioned results are shown in Fig. S3A, and the reasonable energy-level matching provides a potential pathway for electron transfer from $CdIn_2S_4$-NH_2 to MOF-199[39,40].

Furthermore, we recorded the fluorescence spectra of $CdIn_2S_4$ and its mixture with MOF-199 to determine the quenching ability of MOF-199. As shown in Fig. S3B, $CdIn_2S_4$ exhibits fluorescence emission at 500 nm, with the 1028 a.u. fluorescence intensity. However, when $CdIn_2S_4$ is mixed with MOF-199, the fluorescence emission intensity considerably decreases, indicating that MOF-199 inhibits the fluorescence emission of $CdIn_2S_4$.

To further investigate the quenching effect of MOF-199, we performed ECL quenching experiments on $CdIn_2S_4$ using different MOF-199 concentrations (0, 0.5, 1.0, 1.5, 2.0, 2.5, and 3.0 mg/mL) in 10 mL PBS (pH 7.4) containing 80 mmol/L $K_2S_2O_8$ as the co-reactant. The corresponding results are presented in Fig. S3C. With increasing MOF-199 concentration, the ECL intensity progressively decreases (inset of Fig. S3C), illustrating a linear correlation. The quenching constant (K_{sv}) can be evaluated using the Stern–Volmer equation[41,42]: $I_0/I = 1 + K_{sv}[Q]$. In this step, I and I_0 corresponded to the ECL intensity with and without MOF-199, respectively, while [Q] represented the concentration of the MOF-199 quencher. Based on the fitted curve, the correlation coefficient is 0.985 in the range of 0–3.0 mg/mL, and K_{sv} was 3.23×10^6 g^{-1}. The aforementioned results indicate that MOF-199 possesses a substantial quenching effect.

3.3. *Optimization of experimental conditions*

For enhancing the performance of the sandwich-type ECL immunosensor, several key parameters, including the $CdIn_2S_4$ concentration, PBS pH, $K_2S_2O_8$ concentration, and MOF-199 quenching concentration, were optimized. Fig. S4A demonstrates that the maximum ECL intensity is observed at a $CdIn_2S_4$ concentration of 2 mg/mL, after which the ECL intensity decreases owing to impeded electron transfer. The optimal PBS pH for maintaining the bioactivity of the immunosensor was 7.4 (Fig. S4B), and extreme pH values negatively affected the sensor performance. Fig. S4C indicates that the ECL intensity increases with rising $K_2S_2O_8$ concentration up to 80 mmol/L, after which it plateaus, signifying the saturation point and optimal concentration of the co-reactant. Finally, the fabricated immunosensor was utilized for detecting D-dimer at a concentration of 1 ng/mL. Form Fig. S4D, the change in the ECL

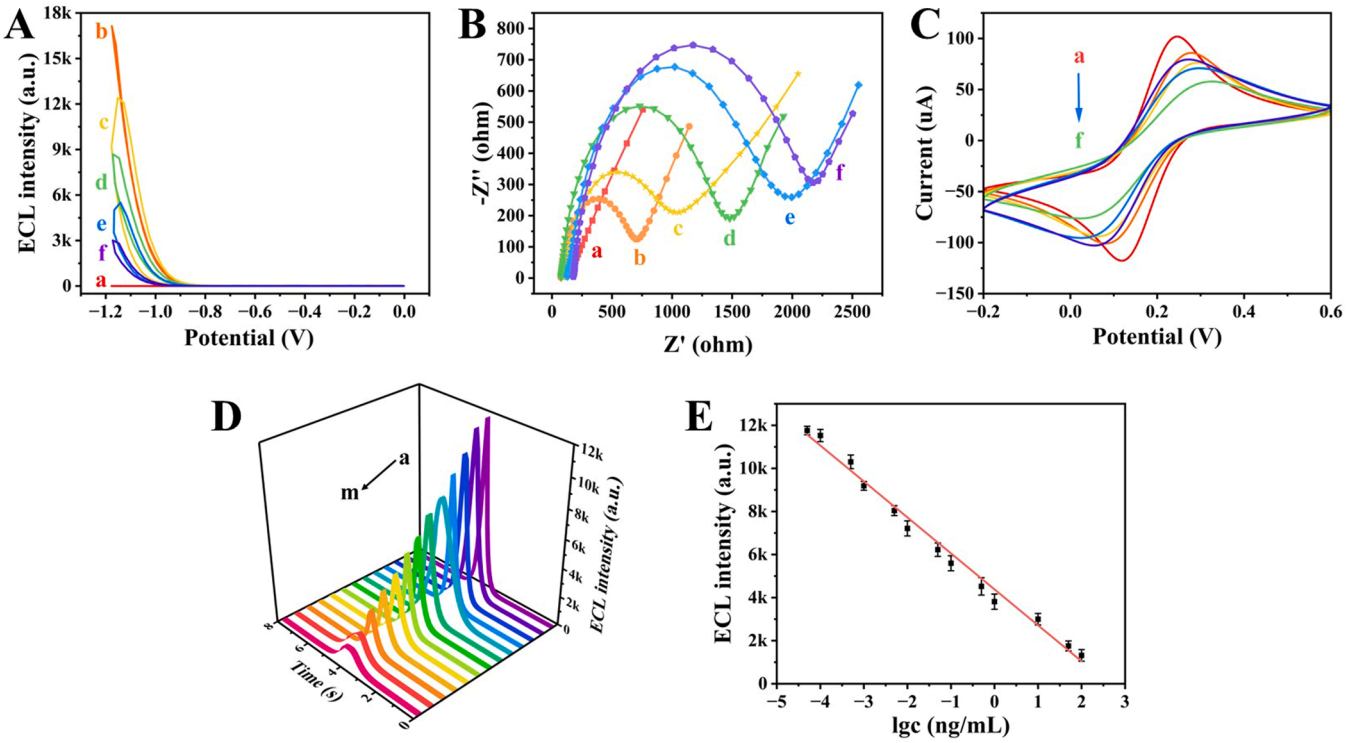

Fig. 4. (A) ECL–V curves of (a) GCE, (b) GCE/$CdIn_2S_4$-NH_2, (c) GCE/$CdIn_2S_4$-NH_2/Ab_1, (d) GCE/$CdIn_2S_4$-NH_2/Ab_1/BSA, (e) GCE/$CdIn_2S_4$-NH_2/Ab_1/BSA/D-dimer, (f) GCE/$CdIn_2S_4$-NH_2/Ab_1/BSA/D-dimer/MOF199-Ab_2 in PBS (pH = 7.4) containing 80 mmol/L $K_2S_2O_8$ and 0.1 mol/L KCl; (B) EIS curves obtained with 2.5 mmol/L $Fe(CN)_6^{3-/4-}$ and 0.1 mol/L KNO_3, and (C) cyclic voltammogram. (D) ECL responses of the immunosensor at different D-dimer concentrations of a to m: 0.00005, 0.0001, 0.0005, 0.001, 0.005, 0.01, 0.05, 0.1, 0.5, 1, 10, 50, and 100 ng/mL. (E) Calibration plot of the immunosensor obtained using different D-dimers. Error bars: ±standard deviation (SD), n = 5.

intensity reaches the maximum at the MOF-199 concentration of 2 mg/mL. Therefore, 2 mg/mL of MOF-199 was determined as the optimal quencher concentration.

3.4. Characterization and performance analysis of the fabricated immunosensor

To validate the immunosensor assembly, the results of the ECL intensity–voltage profile analysis of various modified electrodes are displayed in Fig. 4A. The ECL signal of the bare electrode recorded in PBS (pH 7.4) containing 80 mmol/L $K_2S_2O_8$ was weak (curve a). When the GCE was modified with $CdIn_2S_4$-NH_2, strong ECL emission was obtained at a low excitation potential of −1.18 V (curve b). The low potential facilitated the reduction of energy required for exciting the luminophore and the electrode loss[43,44]. Furthermore, when the GCE was modified with $CdIn_2S_4$-NH_2/Ab_1, the ECL intensity decreased, potentially because the antibody is a macromolecular protein, which is linked to $CdIn_2S_4$-NH_2 through amide bonds, and hinder the electron transfer, leading to signal reduction (curve c). With the continuous step-by-step dropwise addition of BSA and D-dimer (curves d and e, respectively) on to the GCE surface, the ECL intensity gradually decreased, which might be because the obstruction of electron transfer by the protein molecules. Finally, when MOF-199-Ab_2 (curve f) was incubated on the GCE, the ECL signal was minimized because of the ECL quenching effect of MOF-199. These findings confirm the successful fabrication of the immunosensor.

Electrochemical impedance spectroscopy (EIS) was used to evaluate the impedance of the electrodes modified with different materials, demonstrating biosensor assembly. The EIS equivalent circuit is depicted in Fig. 4B, and the corresponding data, simulated using the ZSimpWin software, are presented in Table S1. The diameters of the semicircular arcs in the figure correlate with the electron transfer resistance (Ret) at the electrode-solution interface. Due to the free transfer of electrons, the EIS curve arc of the bare GCE is substantially small and nearly a straight line (curve a). The impedance curve of the GCE modified with $CdIn_2S_4$-NH_2 exhibits a smaller semicircular arc (curve b), indicating the better conductivity of the luminescent substrate material. The modification of the electrode with $CdIn_2S_4$-NH_2/Ab_1 (curve c) increases the arc diameter, and the successive modification of the GCE using BSA (curve d) and D-dimer (curve e) increases the semicircular arc diameter. This is because Ab_1, BSA and D-dimer are non-electroactive substances that impede electron transfer and lead to increased resistance. The continued modification of the electrode with MOF-199-Ab_2 (curve f) further, impedes the electron transfer resulting in the largest arc diameter and maximum Ret value, which confirms the occurrence of a specific recognition reaction between D-dimer and Ab_2. Therefore, the quenching-type ECL immunosensor fabricated in layers is successful. The cyclic voltammogram in Fig. 4C further confirms the successful fabrication of the sensor layer. When the electrode surface is sequentially modified using biomolecules, antibody, BSA, antigen, and Ab_2, the current gradually decreases, indicating the successful fabrication of the sensor.

The performance of the immunosensor was assessed by measuring the ECL intensity at various D-dimer concentrations under optimal conditions. From Fig. 4D, the ECL intensity progressively decreases with increasing D-dimer concentrations from 0.00005 to 100 ng/mL, when assessed under the most favorable experimental conditions. The linear regression equation of the calibration curve (Fig. 4E) was I_{ECL} = 4383.9–1669.7 × lg c, featuring a correlation coefficient of 0.992. Compared with that of other detection schemes (Table S2), the linear detection range of the proposed method was 0.00005 −100 ng/mL, demonstrating a limit of detection (LOD) of 8.51 fg/mL (S/N = 3). The superior performance of the as-developed method compared with the other reported approaches might have originated from the remarkable

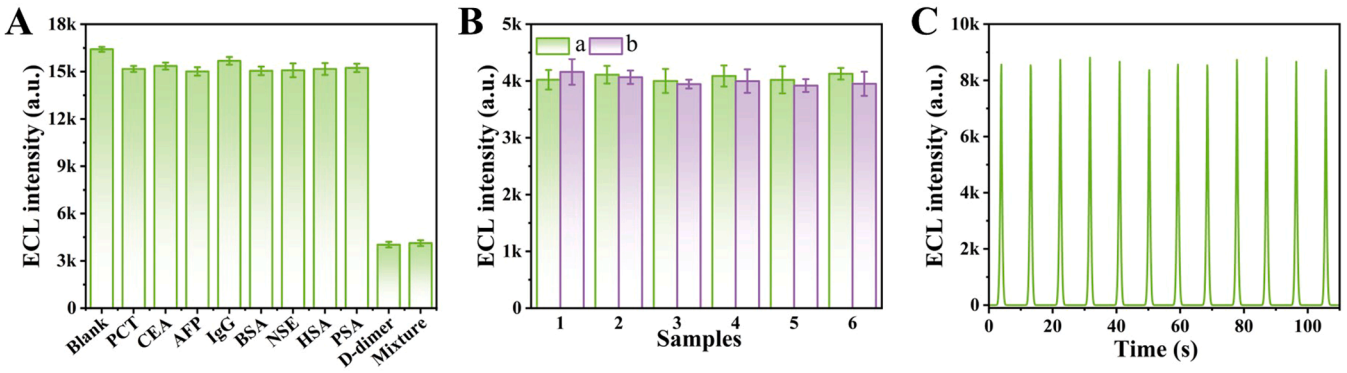

Fig. 5. (A) ECL intensity response of the immunosensor to blank sample, individual interferences (10 ng/mL PCT, CEA, AFP, IgG, BSA, NSE, HSA, and PSA), 1 ng/mL D-dimer, and a mixture of D-dimer (1 ng/mL) with the interfering substances. Error bars: ±standard deviation (SD), n = 5. (B) Reproducibility of D-dimer detection using the immunosensor investigated by (a) intra-batch, and (b) inter-batch analyses. Error bars: ±SD, n = 5. (C) Stability of the ECL immunosensor over 12 cycles.

Table 1
The analysis of D-dimer in human serum samples.

Samples (ng/mL)	Addition (ng/mL)	Average (ng/mL)	Recovery (%)	RSD (% , $n = 11$)
1.5	1.15	2.66	100.9	2.3
	2.34	3.83	99.6	3.2
	4.33	5.82	99.7	1.5
	5.62	7.10	99.6	2.4
3.5	2.56	6.05	99.6	3.4
	3.86	7.35	99.7	2.1
	4.11	7.63	100.5	3.8
	5.85	9.33	99.7	2.7

ECL emission properties of $CdIn_2S_4$-NH_2 and the considerable quenching effect of MOF-199.

3.5. Application performance of the immunosensor

The ECL responses of the immunosensor to various antigens were investigated. Eight common interfering substances in serum were employed to evaluate the selectivity of the immunosensor: namely, procalcitonin (PCT), carcinoembryonic antigen (CEA), alpha-fetoprotein (AFP), immunoglobulin G (IgG), BSA, neuron-specific enolase (NSE), human serum albumin (HSA) and prostate-specific antigen (PSA). As shown in Fig. 5A, the ECL response of the samples added with the test substances, namely, PCT, CEA, AFP, IgG, BSA, NSE, HAS, and PSA, at a concentration of 10 ng/mL, remains nearly unchanged compared with that of the blank sample devoid of any test substances. Furthermore, the ECL response was approximately the same when the sample comprising 1 ng/mL of D-dimer and those composed of 1 ng/mL of D-dimer and the aforementioned interfering substances were used as the detection materials. The aforementioned results indicate that the as-developed ECL immunosensor has good selectivity.

To investigate the reproducibility of the D-dimer immunosensor, we utilized the immunosensor for the intra- and inter-batch detection of D-dimers. As demonstrated in Fig. 5B, intra-analytical precision is assessed by detecting the D-dimer levels in six replicate tests. Inter-analytical precision was determined by detecting the D-dimer levels via six immunosensor assays. The RSD values were 4.37 % and 3.97 %, indicating the good precision and reproducibility, respectively, of the sensor.

Good operational stability is a key factor in the practical detection and analysis applications of immunosensors. From Fig. 5C, the ECL intensity of the immunosensor remains consistent for 12 cycles of the continuous potential detection of D-dimer (0.005 ng/mL) on the working electrode, indicating that the immunosensor has reliable stability with an RSD of 1.75 %.

3.6. Samples analysis

Recovery experiments were performed using the sample spiking recovery method to confirm the precision and accuracy of the fabricated sensor and assess the feasibility of its practical application (Table 1). Human serum samples of known concentrations were diluted to 1.5 and 3.5 ng/mL using PBS (pH = 7.4). Thereafter, a series of D-dimer standard solutions were added to the as-prepared serum samples. The measured recoveries were in the range of 99.6 %−100.9 %, and the relative standard deviations were within 1.5 % − 3.8 % for 11 trials. The aforementioned results indicate that the as-fabricated sensor is promising for application in the detection of D-dimers in serum samples.

4. Conclusion

The advancement of high-performance luminophores and efficient quenchers has considerably accelerated the transition of ECL technology from theoretical concepts to practical applications. Herein, we successfully synthesized a novel ECL emitter $CdIn_2S_4$ whose favorable morphology and bandgap facilitated electron transitions and the formation of excited states, endowing it with exceptional ECL performance. This achievement extends the application of ternary metal sulfides as luminophores in the field of ECL. An efficient quenching probe is essential for enhancing the sensitivity of ECL sensors. Based on a dual-quenching mechanism involving energy and electron transfers, we employed MOF-199 nanomaterials as a quencher to fabricate a quenching-type ECL immunosensor for the highly sensitive quantitative detection of D-dimers. The sensor exhibited excellent linearity within a broad detection range of 0.00005–100 ng/mL and, a detection limit of 8.51 fg/mL (S/N = 3). These findings provide new insights into the clinical applications of ECL technology and offer valuable guidance for the synthesizing of novel luminophores.

CRediT authorship contribution statement

Dan Wu: Software. **Hongmin Ma:** Investigation. **Huangxian Ju:** Software, Investigation. **Qin Wei:** Project administration, Funding acquisition. **Xianpeng Liao:** Software. **Hao Yu:** Data curation. **Lihua Hu:** Writing – review & editing, Funding acquisition. **Kailong Liu:** Investigation. **Fengdi Li:** Writing – original draft, Investigation, Data curation. **Yun Wang:** Investigation.

Declaration of Competing Interest

The authors declare that they have no known competing financial interests or personal relationships that could have appeared to influence the work reported in this paper.

Acknowledgements

This study was supported by the National Natural Science Foundation of China (Nos. 21607055, 22274062), National Key Scientific Instrument and Equipment Development Project of China (No. 21627809).

Appendix A. Supporting information

Supplementary data associated with this article can be found in the online version at doi:10.1016/j.snb.2025.138179.

Data availability

No data was used for the research described in the article.

References

[1] E. Vele, A. Kurtcehajic, E. Zerem, J. Maskovic, E. Alibegovic, A. Hujdurovic, Plasma D-dimer as a predictor of the progression of abdominal aortic aneurysm, J. Thromb. Haemost. 14 (2016) 2298–2303, https://doi.org/10.1111/jth.13487.

[2] J. Favresse, G. Lippi, P.-M. Roy, B. Chatelain, H. Jacqmin, H. ten Cate, F. Mullier, D-dimer: Preanalytical, analytical, postanalytical variables, and clinical applications, Crit. Rev. Clin. Lab. Sci. 55 (2019) 548–577, https://doi.org/10.1080/10408363.2018.1529734.

[3] L. Li, Y. Chen, J.-J. Zhu, Recent advances in electrochemiluminescence analysis, Anal. Chem. 89 (2016) 358–371, https://doi.org/10.1021/acs.analchem.6b04675.

[4] K. Kuang, Y. Lu, Y. Chen, P. Zhang, N. Jia, Double-enhanced sandwich electrochemiluminescence aptasensor based on g-C_3N_4–Au-luminol nanocomposites and ZnCuS nanosheets for highly sensitive detection of mucin 1, Talanta 273 (2024) 125867, https://doi.org/10.1016/j.talanta.2024.125867.

[5] X. Zhang, Y. Jia, R. Feng, T. Wu, N. Zhang, Y. Du, H. Ju, Cucurbituril enhanced electrochemiluminescence of gold nanoclusters via host-guest recognition for sensitive D-dimer sensing, Anal. Chem. 95 (2023) 1461–1469, https://doi.org/10.1021/acs.analchem.2c04463.

[6] T. Shi, L. Hu, J. Chen, Q. Cui, H. Yu, Y. Li, D. Wu, H. Ma, Q. Wei, H. Ju, Dual-quenching electrochemiluminescence system based on resonance energy transfer from gold dendrite@polypyrrole core-shell nanoparticles enhanced g-C_3N_4 to ZnONFs@PDA-sCuO for procalcitonin immunosensing, Sens. Actuators B 371 (2022) 132591, https://doi.org/10.1016/j.snb.2022.132591.

[7] Y. Tang, Y. Liu, Y. Xia, F. Zhao, B. Zeng, Simultaneous detection of ovarian cancer-concerned HE4 and CA125 markers based on Cu single-atom-triggered CdS QDs and Eu MOF@Isoluminol ECL, Anal. Chem. 95 (2023) 4795–4802, https://doi.org/10.1021/acs.analchem.3c00273.

[8] Q. Wu, L. Tian, X. Shan, S. Yang, H. Li, C. Li, R. Chen, J. Lu, An electrochemiluminescence sensor for sensitive detection of malathion based on g-C_3N_4-CdTe composite nanomaterials, Microchim. Acta 189 (2022) 413, https://doi.org/10.1007/s00604-022-05517-w.

[9] M. Lv, X. Cao, M. Tian, R. Jiang, C. Gao, J. Xia, Z. Wang, A novel electrochemical biosensor based on MIL-101-NH_2 (Cr) combining target-responsive releasing and self-catalysis strategy for p53 detection, Biosens. Bioelectron. 214 (2022), https://doi.org/10.1016/j.bios.2022.114518.

[10] A.H. Reshak, Novel photocatalytic water splitting solar-to-hydrogen energy conversion: $CdLa_2S_4$ and $CdLa_2Se_4$ ternary semiconductor compounds, Phys. Chem. Chem. Phys. 20 (2018) 8848–8858, https://doi.org/10.1039/c8cp00373d.

[11] F. Wang, J. Lin, T. Zhao, D. Hu, T. Wu, Y. Liu, Intrinsic “vacancy point defect” induced electrochemiluminescence from coreless supertetrahedral chalcogenide nanocluster, J. Am. Chem. Soc. 138 (2016) 7718–7724, https://doi.org/10.1021/jacs.6b03662.

[12] J. Fang, J. Li, R. Feng, L. Yang, L. Zhao, N. Zhang, G. Zhao, Q. Yue, Q. Wei, W. Cao, Dual-quenching electrochemiluminescence system based on novel acceptor CoOOH@Au NPs for early detection of procalcitonin, Sens. Actuators B 332 (2021) 129544, https://doi.org/10.1016/j.snb.2021.129544.

[13] S. Xiang, J. Li, F. Wang, H. Yang, Y. Jiang, P. Zhang, R. Cai, W. Tan, Novel ultralow-potential electrochemiluminescence aptasensor for the highly sensitive detection of zearalenone using a resonance energy transfer system, Anal. Chem. 95 (2023) 15125–15132, https://doi.org/10.1021/acs.analchem.3c03437.

[14] W. Gong, S. Yang, F. Zhang, F. Tian, J. Chen, Z. Yin, S. Ding, W. Yang, R. Luo, A dual-quenched ECL immunosensor for ultrasensitive detection of retinol binding protein 4 based on luminol@AuPt/ZIF-67 and MnO_2@CNTs, J. Nanobiotechnol. 19 (2021) 272, https://doi.org/10.1186/s12951-021-01020-1.

[15] D. Qin, S. Meng, Y. Wu, G. Mo, B. Deng, Aggregation-induced electrochemiluminescence resonance energy transfer with dual quenchers for the sensitive detection of prostate-specific antigen, Sens. Actuators B 367 (2022) 132176, https://doi.org/10.1016/j.snb.2022.132176.

[16] Y. Li, G. Zhao, B. An, K. Xu, D. Wu, X. Ren, H. Ma, X. Liu, R. Feng, Q. Wei, Multimetal-based metal–organic framework system for the sensitive detection of heart-type fatty acid binding protein in electrochemiluminescence immunoassay, Anal. Chem. 96 (2024) 4067–4075, https://doi.org/10.1021/acs.analchem.3c04515.

[17] L. Zhu, J. Ye, M. Yan, L. Yu, Y. Peng, J. Huang, X. Yang, Sensitive and programmable “signal-off” electrochemiluminescence sensing platform based on cascade amplification and multiple quenching mechanisms, Anal. Chem. 93 (2021) 2644–2651, https://doi.org/10.1021/acs.analchem.0c04839.

[18] X. Dong, G. Zhao, Y. Li, Q. Zeng, H. Ma, D. Wu, X. Ren, Q. Wei, H. Ju, Dual-mechanism quenching of electrochemiluminescence immunosensor based on a novel ECL emitter polyoxomolybdate-zirconia for 17β-estradiol detection, Anal. Chem. 94 (2022) 12742–12749, https://doi.org/10.1021/acs.analchem.2c02350.

[19] Q. Ma, Q. Zhang, T. Maimaiti, S. Lan, X. Liu, Y. Wang, Q. Li, H. Luo, B. Yu, S.-T. Yang, Carbonization reduces the toxicity of metal-organic framework MOF-199 to white-rot fungus Phanerochaete chrysosporium, J. Environ. Chem. Eng. 9 (2021) 106705, https://doi.org/10.1016/j.jece.2021.106705.

[20] H. Li, W. Tong, Z. Yan, L. Li, S. Wang, J. Huo, L. Yang, J. Han, X. Ren, W. Li, Enhanced thermal decomposition and safety of spherical CL-20@MOF-199 composites via micro-nanostructured self-assembly regulation, ACS Appl. Mater. Interfaces 15 (2023) 41850–41860, https://doi.org/10.1021/acsami.3c06732.

[21] B. Zhang, H. Shi, X. Hu, Y. Wang, E. Liu, J. Fan, A novel S-scheme MoS_2/$CdIn_2S_4$ flower-like heterojunctions with enhanced photocatalytic degradation and H_2 evolution activity, J. Phys. D Appl. Phys. 53 (2020) 205101, https://doi.org/10.1088/1361-6463/ab7563.

[22] Y. Zhang, J. Chen, H. Wang, Q. Cui, D. Fan, Y. Zhang, X. Ren, H. Ma, Q. Wei, H. Ju, Novel photoelectrochemical biosensing platform based on a double type II $CdLa_2S_4$/$SnIn_4S_8$/Sb_2S_3 ternary heterojunction as photoactive materials and $NiCo_2O_4$ nanospheres as a photoquencher for CA19-9 detection, Anal. Chem. 94 (2022) 15915–15923, https://doi.org/10.1021/acs.analchem.2c04328.

[23] X. Ma, H. Liu, W. Li, S. Peng, Y. Chen, Reactive adsorption of low concentration methyl mercaptan on a Cu-based MOF with controllable size and shape, RSC Adv. 6 (2016) 96997–97003, https://doi.org/10.1039/c6ra18593b.

[24] X. Yu, Y. Li, Y. Li, S. Liu, Z. Wu, H. Dong, Z. Xu, X. Li, Q. Liu, An electrochemical amplification strategy based on the ferrocene functionalized cuprous oxide superparticles for the detection of NSE, Talanta 236 (2022) 122865, https://doi.org/10.1016/j.talanta.2021.122865.

[25] J. He, B. Li, J. Yu, L. Qiao, S. Li, X. Zu, X. Xiang, Ultra-thin $CdIn_2S_4$ nanosheets with nanoholes for efficient photocatalytic hydrogen evolution, Opt. Mater. 108 (2020) 110231, https://doi.org/10.1016/j.optmat.2020.110231.

[26] L. Gao, Z. Chen, H. Zheng, J. Hu, A distinct hollow spindle-like $CdIn_2S_4$ photocatalyst for high-efficiency tetracycline removal, Mater. Today Chem. 24 (2022) 100800, https://doi.org/10.1016/j.mtchem.2022.100800.

[27] C.-Y. Pei, Y.-G. Chen, L. Wang, W. Chen, G.-B. Huang, Step-scheme WO_3/$CdIn_2S_4$ hybrid system with high visible light activity for tetracycline hydrochloride photodegradation, Appl. Surf. Sci. 535 (2021) 147682, https://doi.org/10.1016/j.apsusc.2020.147682.

[28] L.K. Dhandole, M.A. Mahadik, H.-S. Chung, W.-S. Chae, M. Cho, J.S. Jang, $CdIn_2S_4$ chalcogenide/TiO_2 nanorod heterostructured photoanode: an advanced material for photoelectrochemical applications, Appl. Surf. Sci. 490 (2019) 18–29, https://doi.org/10.1016/j.apsusc.2019.05.222.

[29] J. Huang, L. Li, J. Chen, F. Ma, Y. Yu, Broad spectrum response flower spherical-like composites CQDs@$CdIn_2S_4$/CdS modified by CQDs with up-conversion property for photocatalytic degradation and water splitting, Int. J. Hydrog. Energy 45 (2020) 1822–1836, https://doi.org/10.1016/j.ijhydene.2019.11.078.

[30] S. Guo, Y. Li, C. Xue, Y. Sun, C. Wu, G. Shao, P. Zhang, Controllable construction of hierarchically $CdIn_2S_4$/CNFs/Co_4S_3 nanofiber networks towards photocatalytic hydrogen evolution, Chem. Eng. J. 419 (2021) 129213, https://doi.org/10.1016/j.cej.2021.129213.

[31] X. Guan, Q. Li, T. Maimaiti, S. Lan, P. Ouyang, B. Ouyang, X. Wu, S.-T. Yang, Toxicity and photosynthetic inhibition of metal-organic framework MOF-199 to pea seedlings, J. Hazard. Mater. 409 (2021) 124521, https://doi.org/10.1016/j.jhazmat.2020.124521.

[32] B. Ouyang, F. Liu, C. Liang, J. Zhang, R. Hu, H. Yuan, R. Hai, Y. Yuan, X. Wu, S.-T. Yang, Toxicity and activity inhibition of metal-organic framework MOF-199 to nitrogen-fixing bacterium Azotobacter vinelandii, Sci. Total Environ. 813 (2022) 151912, https://doi.org/10.1016/j.scitotenv.2021.151912.

[33] W. Lai, S. Yan, M. Wang, M. Jiang, X. Liu, J. Li, P. Li, Z. Wei, C. Hong, S–$CdIn_2S_4$: A novel near-infrared emitter triggered by low potential for constructing a dual-mode immunosensing platform, Biosens. Bioelectron. 236 (2023) 115441, https://doi.org/10.1016/j.bios.2023.115441.

[34] W. Zhong, Z. Liang, H. Zhao, P. Wang, Z. Li, J. Shi, Q. Ma, ECL resonance energy transfer-regulated “off-on” mode biosensor for the detection of miRNA-150-5p in triple negative breast cancer, Biosens. Bioelectron. 240 (2023) 115663, https://doi.org/10.1016/j.bios.2023.115663.

[35] Y. Li, Z. Chen, W. Li, F. Zhang, X. Yang, C. Ding, Peptide-antifouling interface for monitoring β-amyloid based on electrochemiluminescence resonance energy transfer, Talanta 267 (2024) 125229, https://doi.org/10.1016/j.talanta.2023.125229.

[36] W. Jiang, M. Zhang, J. Wang, Y. Liu, Y. Zhu, Dramatic visible activity in phenol degradation of TCNQ@TiO_2 photocatalyst with core–shell structure, Appl. Catal. B 160-161 (2014) 44–50, https://doi.org/10.1016/j.apcatb.2014.04.050.

[37] L. Mao, K. Ji, L. Yao, X. Xue, W. Wen, X. Zhang, S. Wang, Molecularly imprinted photoelectrochemical sensor for fumonisin B1 based on GO-CdS heterojunction, Biosens. Bioelectron. 127 (2019) 57–63, https://doi.org/10.1016/j.bios.2018.11.040.

[38] L. Luo, X. Liu, X. Bi, L. Li, T. You, Dual-quenching effects of methylene blue on the luminophore and co-reactant: application for electrochemiluminescent-electrochemical ratiometric zearalenone detection, Biosens. Bioelectron. 222 (2023) 114991, https://doi.org/10.1016/j.bios.2022.114991.

[39] X. Ren, D. Zhang, C. Li, J. Zhao, R. Feng, Y. Zhang, R. Xu, Q. Wei, Europium metal–organic framework with a tetraphenylethylene-based ligand: a dual-mechanism quenching immunosensor for enhanced electrochemiluminescence via

the coordination trigger, Anal. Chem. 96 (2024) 3898–3905, https://doi.org/10.1021/acs.analchem.3c05556.
[40] X. Dong, X. Zhang, Y. Du, J. Liu, Q. Zeng, W. Cao, Q. Wei, H. Ju, Zirconium dioxide as electrochemiluminescence emitter for D-dimer determination based on dual-quenching sensing strategy, Biosens. Bioelectron. 236 (2023) 115437, https://doi.org/10.1016/j.bios.2023.115437.
[41] J. Xue, L. Yang, Y. Jia, Y. Zhang, D. Wu, H. Ma, L. Hu, Q. Wei, H. Ju, Dual-quenching electrochemiluminescence resonance energy transfer system from Ru-In_2S_3 to α-MoO_3-Au based on protect of protein bioactivity for procalcitonin detection, Biosens. Bioelectron. 142 (2019) 111524, https://doi.org/10.1016/j.bios.2019.111524.
[42] S.K. Padhan, N. Murmu, S. Mahapatra, M.K. Dalai, S.N. Sahu, Ultrasensitive detection of aqueous Cu^{2+} ions by a coumarin-salicylidene based AIEgen, Mater. Chem. Front 3 (2019) 2437–2447, https://doi.org/10.1039/c9qm00394k.
[43] Y.-Z. Wang, Y.-R. Li, Y.-Q. Zhang, Y.-M. Xiang, R.-R. Bai, Y. Liu, M.-L. Li, G.-R. Meng, S.-L. Pan, F. Zhang, L. Mi, Y.-H. Hu, Dual-signal ratiometric electrochemiluminescence biosensor based on Au NPs-induced low-potential emission of PFO Pdots and LSPR-ECL mechanism for ultra-sensitive detection of microRNA-141, Biosens. Bioelectron. 261 (2024) 116495, https://doi.org/10.1016/j.bios.2024.116495.
[44] B. Wang, X. Liu, D. Fan, H. Ma, Z. Gao, D. Wu, Q. Wei, Ultrasensitive detection of SARS-CoV-2 nucleocapsid protein based on porphyrin-based metal-organic gels with highly efficient electrochemiluminescence at low potential, Anal. Chem. 96 (2024) 4479–4486, https://doi.org/10.1021/acs.analchem.3c04972.

Fengdi Li studies in school of chemistry and chemical engineering, University of Jinan as postgraduate student.

Yun Wang studies in school of chemistry and chemical engineering, University of Jinan as undergraduate student.

Hao Yu studies in school of chemistry and chemical engineering, University of Jinan as undergraduate student.

Xianpeng Liao studies in school of chemistry and chemical engineering, University of Jinan as postgraduate student.

Kailong Liu studies in school of chemistry and chemical engineering, University of Jinan as postgraduate student.

Lihua Hu received her Ph.D. degree from University of science and technology of China in 2011. Now, she is an associate professor at University of Jinan. Her main research interests focus on the determination of biological targets through chemical sensors.

Hongmin Ma received both his B.S. and M.S. degree in Applied Chemistry from University of Jinan in 2005 and 2008 respectively. And he has received his Ph.D. degree in Colloid and Interface Chemistry at Shandong University, investigating self-assembly at all scales at surfaces in 2011. Now, he is a professor at University of Jinan, interested in the assembly of nano-composites and the construction of ordered porous films as well as their analytical applications.

Dan Wu received the D.S. degree from Shandong University in 2005. Now, she is a professor at University of Jinan. She dedicates to the surfactant and biological macromolecules interaction. And now she also studies the role of surfactant in electrochemical immunosensor.

Qin Wei a professor and DSc, has devoted herself to analytical teaching and scientific research. Her main research interests are the determination of protein and nucleic acid by photometry and the electrochemical immunosensor preparation. She has published over one hundred articles on analysis, immunosensor and applied successfully for many research projects, such as *Biomaterials, Adv. Funct. Mater., Biosens. Bioelectron., Sens. Actuators B: Chem., Talanta.*

Huangxian Ju received his BS, MS and PhD degrees from Nanjing University during 1982–1992, and was a postdoc in Montreal University (Canada) in 1996–1997. He became an associate and full professor of Nanjing University in 1993 and 1999. He is currently the director of State Key Laboratory of Analytical Chemistry for Life Science, Professor of Nanjing University and University of Jinan. His research interests focus on analytical biochemistry, biosensing and molecular diagnosis. He has authored 75 patents (39 approved), 6 English books, 7 Chinese books and 20 chapters, and published 786 papers in different journals with h-index of 100 (Google Scholar h-index 109 with more than 44000 citations).